

Edge conduction in monolayer WTe_2

Zaiyao Fei¹, Tauno Palomaki¹, Sanfeng Wu¹, Wenjin Zhao¹, Xinghan Cai¹, Bosong Sun¹, Paul Nguyen¹, Joseph Finney¹, Xiaodong Xu^{1,2*} and David H. Cobden^{1*}

A two-dimensional topological insulator (2DTI) is guaranteed to have a helical one-dimensional edge mode^{1–11} in which spin is locked to momentum, producing the quantum spin Hall effect and prohibiting elastic backscattering at zero magnetic field. No monolayer material has yet been shown to be a 2DTI, but recently the Weyl semimetal WTe_2 was predicted¹² to become a 2DTI in monolayer form if a bulk gap opens. Here, we report that, at temperatures below about 100 K, monolayer WTe_2 does become insulating in its interior, while the edges still conduct. The edge conduction is strongly suppressed by an in-plane magnetic field and is independent of gate voltage, save for mesoscopic fluctuations that grow on cooling due to a zero-bias anomaly, which reduces the linear-response conductance. Bilayer WTe_2 also becomes insulating at low temperatures but does not show edge conduction. Many of these observations are consistent with monolayer WTe_2 being a 2DTI. However, the low-temperature edge conductance, for contacts spacings down to 150 nm, never reaches values higher than $\sim 20 \mu\text{S}$, about half the predicted value of e^2/h , suggesting significant elastic scattering in the edge.

Experimental work on 2DTIs to date has focused on quantum wells in Hg/CdTe (refs 4–7) and InAs/GaSb (refs 9–11) designed to achieve an inverted bandgap. These heterostructures show edge conduction as anticipated^{13,14}, but they also present some puzzles. One is that the conductance at low temperatures is not perfectly quantized, becoming small in long edges¹³ and showing mesoscopic fluctuations as a function of gate voltage^{5,7,10}. This is inconsistent with the predicted absence of elastic backscattering at zero magnetic field, although several possible explanations have been put forward for the discrepancy^{15–20}. Another is that the edges show signs of conducting even at high magnetic field^{21,22}, contrary to expectations that helical modes, protected by time-reversal (TR) symmetry at zero field, should Anderson-localize once this symmetry is broken. An additional complication is that non-helical edge conduction may also be present, due for instance to band bending when a gate voltage is applied²³.

Identification of a natural monolayer 2DTI would be helpful for elucidating and exploiting TI physics. Band structure calculations predict that certain monolayer materials are topologically nontrivial¹². An example is monolayer WTe_2 , which has the T' structure illustrated in Fig. 1a. Three-dimensional WTe_2 , in which T' monolayers are stacked in the orthorhombic T_d structure, has recently attracted attention as a type-II Weyl semimetal^{24,25} that exhibits an extreme non-saturating magnetoresistance^{26,27} related to the closely balanced electron and hole densities^{28–30}. Calculations suggest that the monolayer will likewise be a semimetal^{12,30}, its Fermi surface comprising two electron pockets (green) and one hole pocket (grey) as shown in Fig. 1b, with areal densities $n = p \approx 1.6 \times 10^{13} \text{ cm}^{-2}$. If this is correct then the helical edge modes

are always degenerate with bulk states (Fig. 1c). In contrast, in a 2DTI the edge modes span a bandgap and cannot be mixed by TR-invariant perturbations, so that they dominate transport when the Fermi energy E_F is in the gap. Here we present evidence that at low temperatures monolayer WTe_2 exhibits an insulating bulk state and edge conduction, and describe the properties of the edge conduction, including its dependence on gate voltage, magnetic field, temperature, contact separation, and bias. We then compare the behaviour with that expected for helical modes with disorder expected to be present at the monolayer edge.

Figure 1f–h shows representative two-terminal measurements of the differential conductance G_{diff} of encapsulated trilayer, bilayer, and monolayer devices, respectively. Each of these devices has a row of contacts along one edge of the WTe_2 sheet, as visible in the optical micrograph of monolayer device MW1 in Fig. 1d. For these particular measurements, two contacts and the gate were connected as shown in Fig. 1e and a small (3 mV) d.c. bias was superposed on the $100 \mu\text{V}$ a.c. excitation. This d.c. bias affects only the lowest temperature measurement (1.6 K), by suppressing a zero-bias anomaly (ZBA) of uncertain origin, as will be explained later.

On cooling from 300 K the trilayer (Fig. 1f) shows metallic behaviour at all V_g , the conductance rising steadily before saturating at the lowest temperatures, consistent with the behaviour²⁶ of bulk WTe_2 . The bilayer (Fig. 1g) develops a strong V_g dependence with a sharp minimum near $V_g = 0$, while remaining metallic at large V_g . The minimum drops steadily and below ~ 20 K it broadens and reproducible mesoscopic fluctuations appear. The monolayer (Fig. 1h) first develops a similar but wider minimum, but below ~ 100 K the minimum stops dropping and instead broadens into a plateau of conductance, here at $\sim 16 \mu\text{S}$, on which there are mesoscopic fluctuations. The inset to Fig. 1f compares the temperature dependence in the three cases. We will show below that the plateau seen only in the monolayer is due to edge conduction remaining when the bulk becomes insulating below ~ 100 K.

Edge conduction is normally detected using nonlocal measurements⁶ such as those shown in Fig. 2b. Here we apply a small excitation V_0 between contacts 2 and 6 on opposite edges of monolayer device MW2 (Fig. 2a, left image) that has approximate Hall-bar geometry, and we detect the nonlocal voltage V_{nl} induced between contacts 4 and 5 which are far out of the normal current path. At low T and small V_g , V_{nl}/V_0 grows large, suggesting that in this regime most of the current follows the edge. At higher T or larger V_g , V_{nl}/V_0 falls off as more current takes the direct path through the bulk.

Although this measurement indicates that the current follows the edge, the shape of the WTe_2 flake in device MW2 is unsuitable for quantitative separation of bulk and edge contributions. To address this, we designed monolayer device MW3 (Fig. 2a, right image) which employs a series of alternating pincer-shaped contacts

¹Department of Physics, University of Washington, Seattle, Washington 98195, USA. ²Department of Materials Science and Engineering, University of Washington, Seattle, Washington 98195, USA. *e-mail: xuxd@uw.edu; cobden@uw.edu

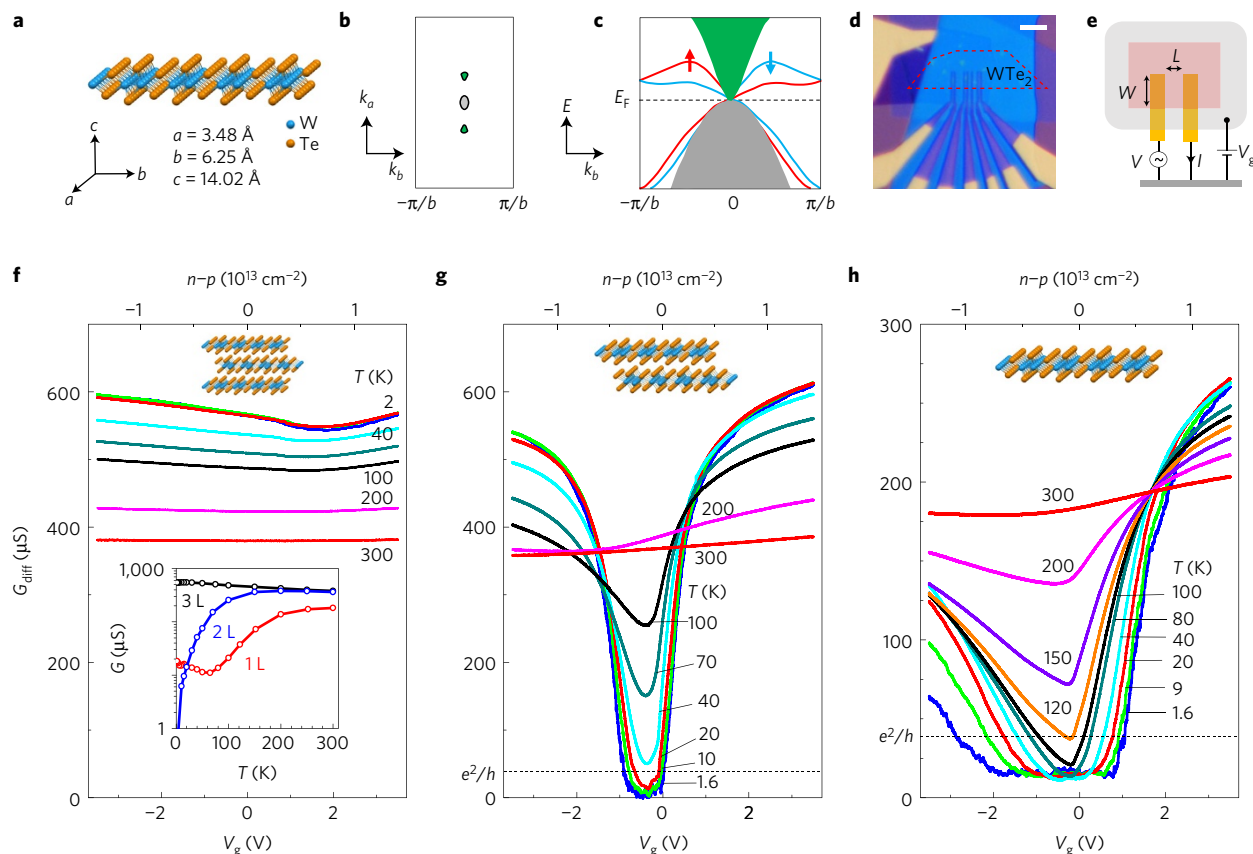


Figure 1 | Two-terminal characteristics of WTe₂ devices. **a**, Structure and lattice constants of monolayer WTe₂. Tungsten atoms form zigzag chains along the *a*-axis. **b**, Sketch of its calculated Fermi surface, showing two electron (green) and one hole (grey) pockets. **c**, Sketch of calculated bands in a strip of monolayer WTe₂. The spin-resolved helical edge modes (red and blue lines) are predicted to be degenerate with bulk states (grey and green) at all energies. **d**, Optical image of monolayer WTe₂ device MW1. Scale bar, 5 μm. **e**, Schematic two-terminal measurement configuration, indicating also the voltage applied to the few-layer graphene top gate (grey). The pink region is the monolayer WTe₂. **f–h**, Temperature dependence of the characteristics for similar contact pairs on a trilayer ($L = 0.20 \mu\text{m}$, $W = 3.4 \mu\text{m}$), bilayer ($L = 0.26 \mu\text{m}$, $W = 3.1 \mu\text{m}$), and monolayer ($L = 0.24 \mu\text{m}$, $W = 3.3 \mu\text{m}$) device (MW1), respectively. Here the differential conductance G_{diff} is measured with a small (3 mV) d.c. bias to suppress effects of a zero-bias anomaly in the 1.6 K sweep for the monolayer. The inset to **f** compares the temperature dependence of the conductance minimum in the three cases.

overlapping one straight edge of a monolayer flake, as shown schematically in the insets to Fig. 2c. The two-terminal linear conductance between a pair of pincers (black trace in Fig. 2c), here at 10 K, behaves similarly to a pair of adjacent contacts in device MW1 (Fig. 1h). However, if the smaller rectangular contact interposed between them is grounded (blue trace in Fig. 2c), so that any current flowing near the edge is shorted out, I/V is suppressed nearly to zero around $V_g = 0$. This confirms that around $V_g = 0$ most of the current flows near the edge. However, for V_g larger than about ± 2 V, conduction does occur through the two-dimensional bulk, directly across the gap between the pincers. Figure 2d shows measurements of the same quantity at 1.6 K, on a logarithmic scale, both with (green trace) and without (blue trace) a perpendicular magnetic field $B_{\perp} = 10$ T. Near $V_g = 0$ at this temperature the bulk conductance is unmeasurably small. Below ~ 100 K it is approximately activated, while above it rises roughly linearly with T (see Supplementary Information 5). The effect of the perpendicular magnetic field is small; the same is true for an in-plane magnetic field.

In Fig. 2e the black trace is a measurement at zero magnetic field between two adjacent contacts, using the configuration shown in the inset where the rightmost contact (not shown) is grounded to eliminate current along paths not directly between the adjacent contacts. The blue trace is the same measurement done with an in-plane field B_{\parallel} of 14 T. Since the bulk conductivity is almost immune to magnetic field, the decrease in I/V must be associated with the edge. Near $V_g = 0$, where the bulk is insulating, I/V drops nearly

to zero, implying that the edge conduction is strongly suppressed by the magnetic field. In addition, the magnitude of the drop, plotted in red, is similar at all V_g . This implies that the edge makes a roughly constant contribution to the conductance, independent of gate voltage and bulk conductivity.

The edge conduction can be isolated by working at T and V_g low enough that bulk conduction is negligible, corresponding for example to the plateau region in Fig. 1h. Then the section of edge between each pair of adjacent contacts behaves as an independent two-terminal conductor. This is demonstrated by the effect of grounding the central contact shown in Fig. 2c, and also by the fact that 2- and 4-terminal measurements on an edge in this regime give identical results (Supplementary Information 3). Figure 3 shows the effects of magnetic field and temperature on the linear-response conductance between two adjacent contacts in device MW2, which we call G_{edge} to emphasize that there is negligible bulk contribution. Figure 3a shows the T dependence at zero field. On cooling from 50 K to 10 K, G_{edge} increases, but below ~ 10 K at typical V_g it decreases again as the mesoscopic oscillations grow. The inset shows the T dependence at a particular V_g where G_{edge} stays level below 10 K. Figure 3b shows the effect of B_{\parallel} , oriented as shown in the inset to Fig. 3c, at 1.6 K. Figure 3c shows B_{\parallel} sweeps at $V_g = 0$ for a series of temperatures. At moderate B_{\parallel} and T the behaviour approximates the activated function $G_{\text{edge}} = G_0 e^{-\alpha B_{\parallel}/T}$, where $G_0 = 17 \mu\text{S}$ and $\alpha = 5$, plotted as the red dashed lines. The effect of perpendicular field (B_{\perp}) is similar but weaker, as illustrated in the lower inset.

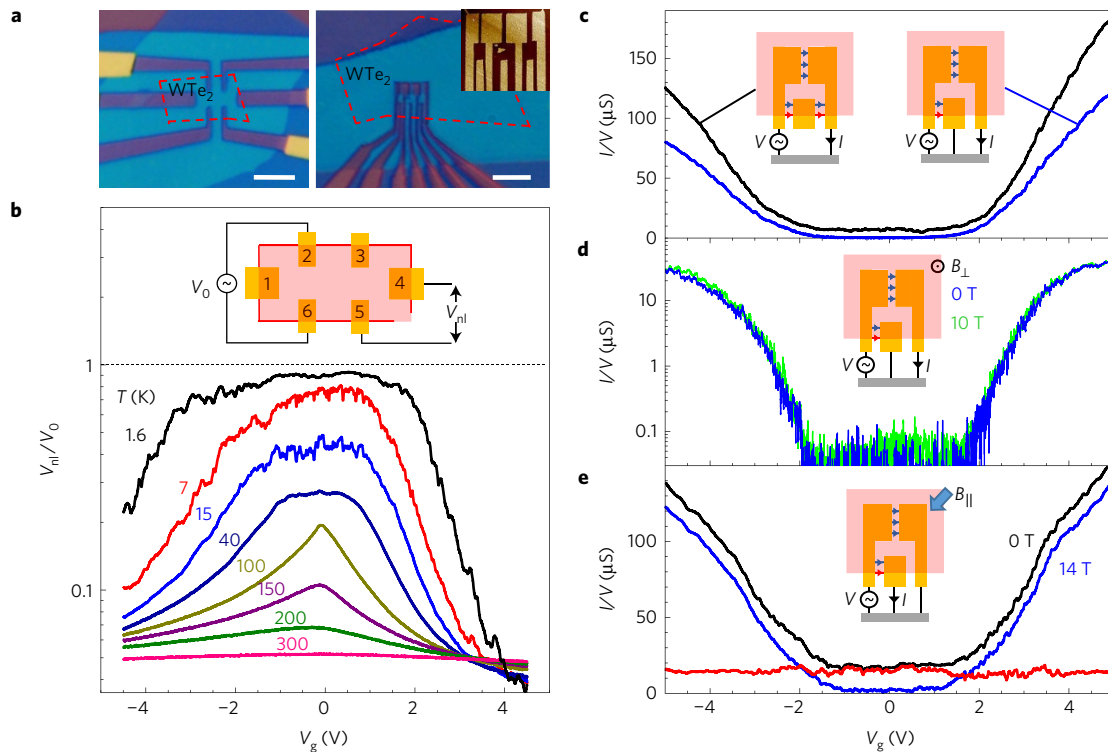


Figure 2 | Distinguishing edge and bulk conduction. **a**, Optical images of the electrodes for monolayer devices MW2 (left) with a Hall-bar layout and MW3 (right) designed to distinguish edge and bulk contributions. Red dashed lines show positions of the monolayer sheets transferred onto them. Scale bars are 5 μm . Inset: AFM image of the electrodes. **b**, Nonlocal measurements on device MW2 in the configuration shown in the inset ($V_0 = 100 \mu\text{V}$ at 11.3 Hz). **c–e**, Measurements on MW3 (the contact separation along the edge is 0.22 μm ; the pincer spacing is 0.28 μm). **c**, As indicated by the insets, the black trace is the two-terminal conductance between the outer contacts and the blue trace is I/V measured with the centre contact grounded ($T = 10 \text{K}$). In the insets, red and blue arrows indicate edge and bulk current paths, respectively. **d**, Same measurement as for the blue trace in **c** but at 1.6 K, on a logarithmic scale, showing the very weak effect of a perpendicular magnetic field of 10 T. **e**, Effect of in-plane magnetic field $B_{||} = 14 \text{T}$ on I/V between adjacent contacts ($T = 10 \text{K}$). The red trace is the magnitude of the decrease.

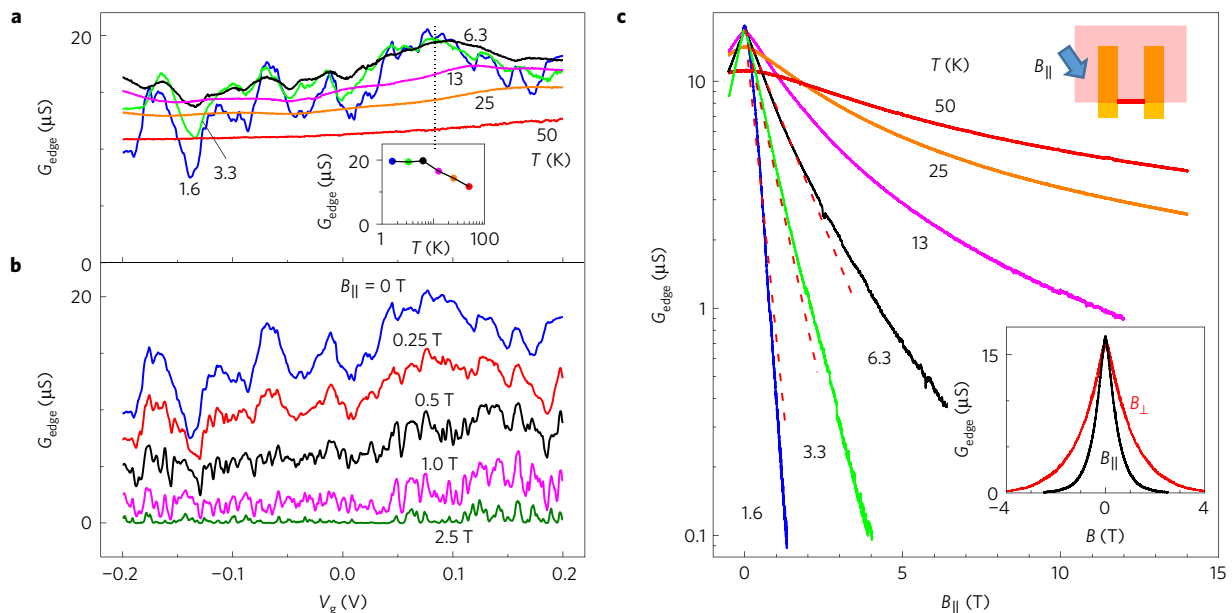


Figure 3 | Temperature and magnetic field dependence of the edge conduction. **a**, Temperature dependence of the conductance G_{edge} between adjacent contacts versus gate voltage at zero magnetic field. (Device MW2, $L = 1.3 \mu\text{m}$, $V = 100 \mu\text{V}$ a.c.) Inset: T dependence at $V_g = +0.08 \text{V}$. **b**, Effect of in-plane magnetic field $B_{||}$ at 1.6 K. **c**, Sweeps of $B_{||}$ at $V_g = 0$ for various temperatures. Dashed lines plot $G_0 \exp(-\alpha B/T)$ with $G_0 = 17 \mu\text{S}$, $\alpha = 5$. Upper inset: orientation of $B_{||}$ relative to the edge. Lower inset: Comparing perpendicular and in-plane fields at 1.6 K ($V_g = 0$).

The edge conduction is often highly nonlinear at small biases. Figure 4a shows a typical $I-V$ curve at $B_{||} = 0$ (black) and at 10 T (blue). Figure 4b shows the corresponding differential conductance.

At $B_{||} = 0$ there is a sharp dip in dI/dV at $V = 0$, or zero-bias anomaly³¹ (ZBA), whereas at 10 T there is a sharp threshold for current flow. All edges show some dip at 1.6 K, but its size varies

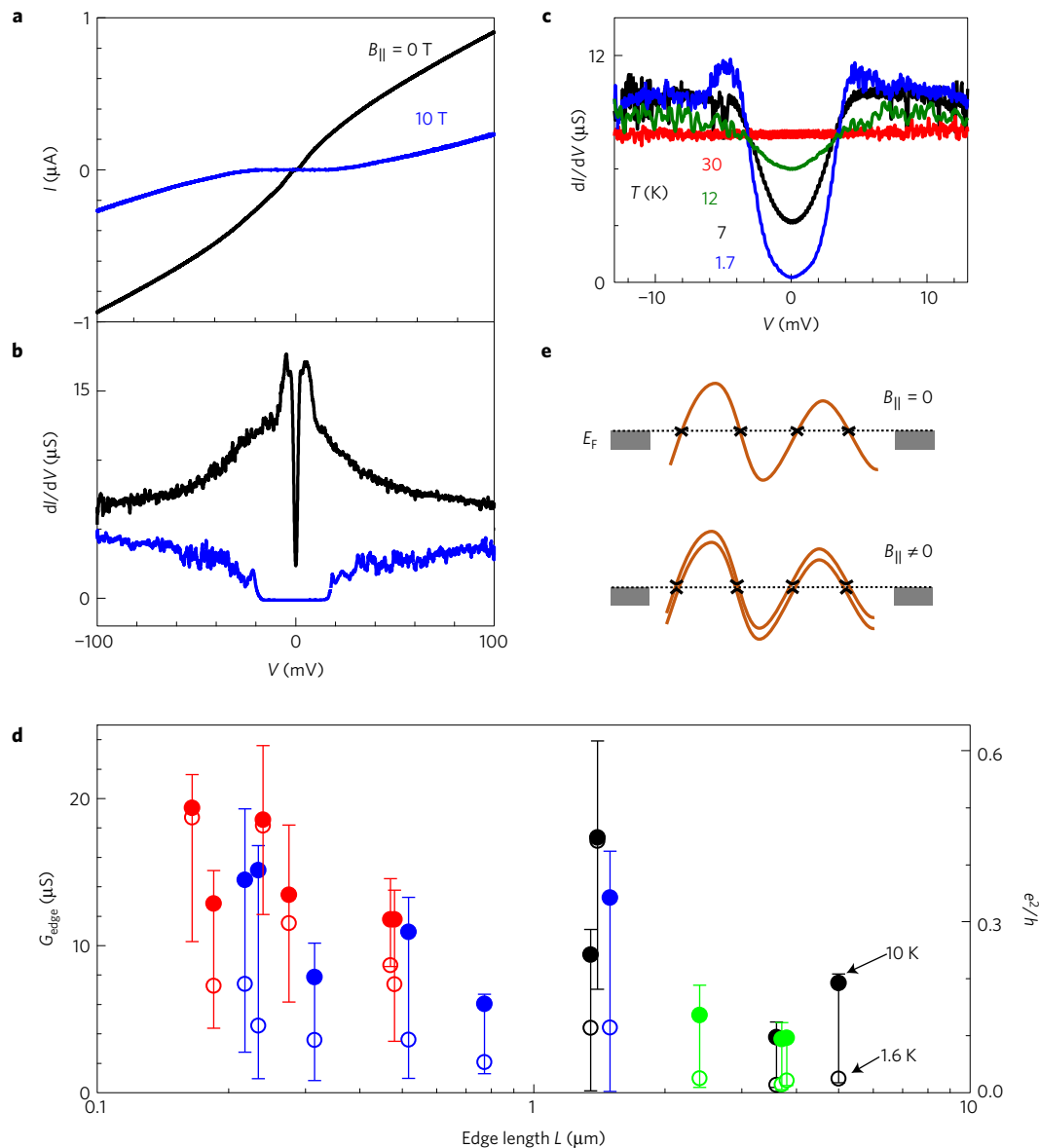


Figure 4 | Statistics, nonlinear properties, and simple picture of edge conduction. **a**, I - V curves at $B_{\parallel} = 0$ (black) and 10 T (blue) for device MW1, $L = 1.5 \mu\text{m}$ ($V_g = 0$, $T = 1.6$ K). **b**, Corresponding differential conductance. A zero-bias anomaly (ZBA) is seen at $B_{\parallel} = 0$. **c**, Temperature dependence of the ZBA at $V_g = -0.68$ V. **d**, Gate-averaged linear-response edge conductance for 19 adjacent-contact pairs (blue, device MW1; black, MW2; red, MW3; green, MW4) at 10 K (solid circles) and 1.6 K (open circles). The error bars in each case show the full range of values spanned by the mesoscopic fluctuations. **e**, Cartoon picture of combined effects of smooth static disorder and a magnetic field-induced gap along the edge.

between different edges and as a function of V_g . It always deepens as T decreases, as illustrated in Fig. 4c. The mesoscopic fluctuations that grow on cooling are linked to the ZBA. When a small d.c. bias is applied to suppress the anomaly, the fluctuations are also suppressed and we see a flatter edge conduction plateau, which is more representative of the generic behaviour of all devices factoring out the ZBA. This is why in Fig. 1 we plotted $G_{\text{diff}} = dI/dV$ at $V = 3$ mV.

In Fig. 4d we compile measurements for 19 adjacent-contact pairs in four different monolayer devices, colour coded by device, at zero magnetic field. The edge length L , which ranges from 0.16 to 5.5 μm , was estimated from atomic force microscope (AFM) images. For each edge we show the linear conductance, averaged over a window of V_g in which the bulk contribution is negligible, at 10 K (solid circles) and 1.6 K (open circles). At both temperatures the average conductance tends to decrease with L , but the trend is rather weak compared with the large, seemingly random variations. The edges

with the weakest T dependence in this range also have the highest conductance, $\sim 20 \mu\text{S}$.

We now discuss the compatibility of the above observations with the scenario of a helical edge mode, in comparison with a trivial edge mode or carrier accumulation due to band bending. First, the monolayer edge conductance is roughly independent of V_g , and therefore chemical potential, over the entire accessible range (Fig. 2e). This is consistent with a single gapless mode, and not with carrier accumulation due to band bending or a trivial edge mode. Second, we see no edge conduction in bilayers (Fig. 1g). This can be explained by the fact that TR symmetry does not prohibit backscattering at the bilayer edge if the electron changes layer (the pair of coupled edges is not helical), whereas band-bending effects should be similar to those in a monolayer. Third, the conductance is dramatically suppressed by B_{\parallel} (Fig. 3c), consistent with the expectation that elastic backscattering is allowed once TR symmetry is broken.

It is also in keeping with a single mode that the linear edge conductance G_{edge} never exceeds the quantized value of $e^2/h = 38.7 \mu\text{S}$ expected in the low-temperature limit when elastic backscattering is completely prohibited (Fig. 4d). It is also encouraging that conductance of this order can occur for micron-scale edges in spite of potentially strong disorder at the torn edge of the exfoliated monolayer. On the other hand, even when the T dependence is small and for the shortest edges, G_{edge} reaches only about half e^2/h at a peak. One possible factor is imperfect transmission between the metal contacts and the edge. (Spin relaxation in the metal contacts when current is exchanged with a helical edge might play a role.) Another is backscattering from multiple magnetic impurities^{16–19} or puddles in the disorder potential²⁰, suggested to explain deviations from quantization observed in the quantum well systems. If some form of backscattering is allowed at points in a quantum wire it is natural for a ZBA to develop due to interaction effects, such as occurs in a helical Luttinger liquid^{32–34}. Nevertheless, we do not observe the quantized conductance that would be a definitive signature of a 2DTI.

The approximately activated behaviour, $e^{-\alpha B_{\parallel}/T}$, in an in-plane magnetic field suggests the opening of a gap, $\Delta_{\text{B}} = g\mu_{\text{B}}B_{\parallel}$, resulting in some form of hopping conduction. Here μ_{B} is the Bohr magneton and $g = \alpha k_{\text{B}}/\mu_{\text{B}} \approx 7.5$ is an effective g -factor. In hopping there are many possible mechanisms for magnetoresistance^{35,36}, but some are ruled out by the atomic-scale thinness of the sample and by the relatively weak dependence on V_{g} . The following simple picture captures most of the observed behaviour.

We suppose that there is indeed a single helical edge mode that follows the physical edge of the monolayer and effectively experiences a large but smooth disorder potential, for example due to fixed charges. As a result, the energy at which the left- and right-going branches are degenerate fluctuates up and down along the edge, passing through E_{F} at multiple points. This situation is sketched in Fig. 4e. If some inter-branch scattering is possible in spite of the helical protection, it is likely to be strongest at these ‘weak points’ where no momentum transfer is required. At $B_{\parallel} = 0$ in some edges the average linear conductance G_{edge} is not much less than e^2/h , and so the scattering must be weak, yet we see large, rapid mesoscopic fluctuations (Fig. 3a). If the origin of these fluctuations is quantum interference, then since no Feynman paths enclose magnetic flux in a one-dimensional wire we expect no corresponding fluctuations as a function of B_{\perp} , as is the case (see Fig. 3c inset). As T decreases, the scattering from the weak points strengthens at energies near E_{F} due to interaction effects^{37,38}, producing the ZBA. Edges longer than a few hundred nanometres (see Fig. 4d) are not phase-coherent and so have smaller conductance due to classical addition of resistance. Also, as T rises the coherence length will decrease, consistent with the fact that G_{edge} tends to decrease with T when the ZBA is small (see Fig. 3a, above ~ 6 K). A magnetic field opens a gap Δ_{B} in the helical modes, as sketched in the lower part of Fig. 4e. Electrons at E_{F} now encounter this gap at the weak points, which they can pass by activation, thus introducing the factor $e^{-\Delta_{\text{B}}/k_{\text{B}}T}$ in the conductance.

We note that the bulk insulating behaviour seen in monolayers below ~ 100 K (see Fig. 2d and Supplementary Information 5) could involve electron–hole correlations, as for example in an excitonic insulator^{39,40}, but it is hard to study quantitatively by standard transport techniques because of the edge conduction. If monolayer WTe_2 is indeed a 2DTI, with helical edge conduction at temperatures as high as 100 K, it will afford new opportunities in the realms of topological and low-dimensional science. On the one hand, unlike the electrostatic confinement in quantum wells the edge of an exfoliated monolayer is abrupt, and its orientation, roughness, and chemical details are important, especially for mesoscopic effects. Control of these factors may be possible by passivation or epitaxial growth⁴¹. On the other hand, the band structure can be tuned by chemical substitution or applying strain, and the electronic properties can be probed by surface techniques

such as scanning tunnelling spectroscopy. As a monolayer it can also be combined with layered magnets, semiconductors, and superconductors; for example, to manipulate spin polarization or to create Majorana modes^{3,42}.

Methods

Methods, including statements of data availability and any associated accession codes and references, are available in the [online version of this paper](#).

Received 7 October 2016; accepted 10 March 2017;
published online 10 April 2017

References

- Kane, C. & Mele, E. A new spin on the insulating state. *Science* **314**, 1692–1693 (2006).
- Hasan, M. Z. & Kane, C. L. Colloquium: topological insulators. *Rev. Mod. Phys.* **82**, 3045–3067 (2010).
- Qi, X.-L. & Zhang, S.-C. Topological insulators and superconductors. *Rev. Mod. Phys.* **83**, 1057–1110 (2011).
- Bernevig, B. A., Hughes, T. L. & Zhang, S.-C. Quantum spin Hall effect and topological phase transition in HgTe quantum wells. *Science* **314**, 1757–1761 (2006).
- König, M. *et al.* Quantum spin Hall insulator state in HgTe quantum wells. *Science* **318**, 766–770 (2007).
- Roth, A. *et al.* Nonlocal transport in the quantum spin Hall state. *Science* **325**, 294–297 (2009).
- Gusev, G. M. *et al.* Transport in disordered two-dimensional topological insulators. *Phys. Rev. B* **84**, 121302(R) (2011).
- König, M. *et al.* Spatially resolved study of backscattering in the quantum spin Hall state. *Phys. Rev. X* **3**, 021003 (2013).
- Knez, I., Du, R.-R. & Sullivan, G. Evidence for helical edge modes in inverted InAs/GaSb quantum wells. *Phys. Rev. Lett.* **107**, 136603 (2011).
- Suzuki, K., Harada, Y., Onomitsu, K. & Muraki, K. Edge channel transport in the InAs/GaSb topological insulating phase. *Phys. Rev. B* **87**, 235311 (2013).
- Li, T. *et al.* Observation of a helical Luttinger liquid in InAs/GaSb quantum spin Hall edges. *Phys. Rev. Lett.* **115**, 136804 (2015).
- Qian, X., Liu, J., Fu, L. & Li, J. Quantum spin Hall effect in two-dimensional transition metal dichalcogenides. *Science* **346**, 1344–1347 (2014).
- Nowack, K. C. *et al.* Imaging currents in HgTe quantum wells in the quantum spin Hall regime. *Nat. Mater.* **12**, 787–791 (2013).
- Spanton, E. M. *et al.* Images of edge current in InAs/GaSb quantum wells. *Phys. Rev. Lett.* **113**, 026804 (2014).
- Xu, C. & Moore, J. E. Stability of the quantum spin Hall effect: effects of interactions, disorder, and Z_2 topology. *Phys. Rev. B* **73**, 045322 (2006).
- Maciejko, J. *et al.* Kondo effect in the helical edge liquid of the quantum spin Hall state. *Phys. Rev. Lett.* **102**, 256803 (2009).
- Tanaka, Y., Furusaki, A. & Matveev, K. A. Conductance of a helical edge liquid coupled to a magnetic impurity. *Phys. Rev. Lett.* **106**, 236402 (2011).
- Alshuler, B. L. *et al.* Localization at the edge of a 2D topological insulator by Kondo impurities with random anisotropies. *Phys. Rev. Lett.* **111**, 086401 (2013).
- Cheianov, V. & Glazman, L. I. Mesoscopic fluctuations of conductance of a helical edge contaminated by magnetic impurities. *Phys. Rev. Lett.* **110**, 206803 (2013).
- Väyrynen, J. I. *et al.* Resistance of helical edges formed in a semiconductor heterostructure. *Phys. Rev. B* **90**, 115309 (2014).
- Du, L., Knez, I., Sullivan, G. & Du, R.-R. Robust helical edge transport in gated InAs/GaSb bilayers. *Phys. Rev. Lett.* **114**, 096802 (2015).
- Ma, E. Y. *et al.* Unexpected edge conduction in mercury telluride quantum wells under broken time-reversal symmetry. *Nat. Commun.* **6**, 7252 (2015).
- Vera-Marun, I. J. *et al.* Quantum Hall transport as a probe of capacitance profile at graphene edges. *Appl. Phys. Lett.* **102**, 013106 (2013).
- Soluyanov, A. A. *et al.* Type-II Weyl semimetals. *Nature* **527**, 495–498 (2015).
- Wu, Y. *et al.* Observation of Fermi arcs in the type-II Weyl semimetal candidate WTe_2 . *Phys. Rev. B* **94**, 121113 (2016).
- Ali, M. N. *et al.* Large, non-saturating magnetoresistance in WTe_2 . *Nature* **514**, 205–208 (2014).
- Zhao, Y. F. *et al.* Anisotropic magnetotransport and exotic longitudinal linear magnetoresistance in WTe_2 crystals. *Phys. Rev. B* **92**, 206803(R) (2015).
- Pletikosic, I., Ali, M. N., Fedorov, A. V., Cava, R. J. & Valla, T. Electronic structure basis for the extraordinary magnetoresistance in WTe_2 . *Phys. Rev. Lett.* **113**, 216601 (2014).
- Cai, P. L. *et al.* Drastic pressure effect on the extremely large magnetoresistance in WTe_2 : quantum oscillation study. *Phys. Rev. Lett.* **115**, 057202 (2015).

30. Lv, H. Y. *et al.* Perfect charge compensation in WTe_2 for the extraordinary magnetoresistance: from bulk to monolayer. *Europhys. Lett.* **110**, 37004 (2015).
31. Altshuler, B. L. & Aronov, A. G. Zero bias anomaly in tunnel resistance and electron-electron interaction. *Solid State Commun.* **30**, 115–117 (1979).
32. Wu, C. J., Bernevig, B. A. & Zhang, S. C. Helical liquid and the edge of quantum spin Hall systems. *Phys. Rev. Lett.* **96**, 106401 (2006).
33. Schmidt, T. L., Rachel, S., von Oppen, F. & Glazman, L. I. Inelastic electron backscattering in a generic helical edge channel. *Phys. Rev. Lett.* **108**, 156402 (2012).
34. Väyrynen, J. I., Geissler, F. & Glazman, L. I. Magnetic moments in a helical edge can make weak correlations seem strong. *Phys. Rev. B* **93**, 241301(R) (2016).
35. Bahlouli, H., Matveev, K. A., Ephron, D. & Beasley, M. R. Coulomb correlations in hopping through a thin layer. *Phys. Rev. B* **49**, 14496–14503 (1994).
36. Ioffe, L. B. & Spivak, B. Z. Giant magnetoresistance in the variable-range hopping regime. *J. Exp. Theor. Phys.* **117**, 551–569 (2013).
37. Kane, C. L. & Fisher, M. P. A. Transport in a one-channel Luttinger liquid. *Phys. Rev. Lett.* **68**, 1220–1223 (1992).
38. Furusaki, A. & Nagaosa, N. Single-barrier problem and Anderson localization in a one-dimensional interacting electron system. *Phys. Rev. B* **47**, 4631–4643 (1993).
39. Kohn, W. Excitonic phases. *Phys. Rev. Lett.* **19**, 439–442 (1967).
40. Cercellier, H. *et al.* Evidence for an excitonic insulator phase in 1T-TiSe₂. *Phys. Rev. Lett.* **99**, 146403 (2007).
41. Huang, C. M. *et al.* Lateral heterojunctions within monolayer MoSe₂-WSe₂ semiconductors. *Nat. Mater.* **13**, 1096–1101 (2014).
42. Fu, L. & Kane, C. L. Superconducting proximity effect and majorana fermions at the surface of a topological insulator. *Phys. Rev. Lett.* **100**, 096407 (2008).

Acknowledgements

We thank J. Yan (Oak Ridge National Laboratory) for providing the WTe_2 crystals, and A. Andreev, L. Glazman, J. Maciejko, K. Matveev, J. Moore, B. Spivak, J. Väyrynen and D. Xiao for discussions. The major part of this work was supported by the US Department of Energy, Office of Basic Energy Sciences, Division of Materials Sciences and Engineering, Awards DE-SC0002197 (D.H.C.) and DE-SC0012509 (X.X.). T.P. and Z.F. were supported by AFOSR FA9550-14-1-0277. P.N., J.F. and some facilities were supported by NSF EFRI 2DARE 1433496.

Author contributions

D.H.C. and X.X. conceived the experiment; Z.F., T.P., S.W. and D.H.C. performed the measurements; Z.F., W.Z., S.W., T.P., X.C., B.S., P.N. and J.F. fabricated the devices; D.H.C., X.X., Z.F. and T.P. analysed the results; and D.H.C., Z.F., T.P. and X.X. wrote the paper with comments from all authors.

Additional information

Supplementary information is available in the [online version of the paper](#). Reprints and permissions information is available online at www.nature.com/reprints. Publisher's note: Springer Nature remains neutral with regard to jurisdictional claims in published maps and institutional affiliations. Correspondence and requests for materials should be addressed to X.X. or D.H.C.

Competing financial interests

The authors declare no competing financial interests.

Methods

Device fabrication. hBN crystals were mechanically exfoliated under ambient conditions onto substrates consisting of 285 nm thermal SiO₂ on highly *p*-doped silicon. 14–30-nm-thick hBN flakes were used for the lower dielectric and 5–12-nm-thick flakes for the upper dielectric (see Supplementary Table 1 in Supplementary Information 1 for details). Pt or Pd metal contacts (no substantial difference was found between these two metals) were deposited at ~5 nm thickness on the lower hBN by standard e-beam lithography and metallized in an e-beam evaporator followed by acetone lift-off. The upper hBN was picked up using a polymer-based dry transfer technique⁴³ and then moved into a glove box with oxygen level below 0.5 ppm along with the lower hBN/contact structure. Flux-grown WTe₂ crystals²⁷ were exfoliated inside the glove box and a monolayer flake was optically identified and quickly picked up with the upper hBN before transferring onto the lower hBN/contacts to complete the stack. Thus the WTe₂ was fully encapsulated before removing from the glove box. After dissolving the polymer, a few-layer (3–5 nm thick) graphene flake was transferred onto the BN/WTe₂/BN stack as a top gate (except for device MW2, in which the top gate was transferred after the last metallization process). Finally, another step of e-beam lithography and metallization (Au/V) was used to define wire-bonding pads connecting to the metal contacts and the top gate.

In all the measurements presented, we only biased the top gate to V_g , while the substrate gate was grounded. Assuming the electron/hole density of states is not too small, the change in electron–hole density imbalance simply depends on the capacitance, $\Delta(n-p) = C_{ig} \Delta V_g / e$. Here C_{ig} is the areal capacitance corresponding to the top gate, $C_{ig} = \epsilon_r \epsilon_0 / d_{hBN}$, where $\epsilon_r \approx 4$ for hBN (ref. 44) and d_{hBN} is the thickness of the upper hBN flake.

Conductance measurements. The conductance measurements shown in Figs 2 and 3 and in Supplementary Information 8 were made with a 100 μ V a.c. excitation

at 11.3 Hz and no d.c. bias, that is, in linear response. In MW1 and MW3, at low temperature and small gate voltages, conduction was found to be entirely along the shorter edge between the contacts. Conduction along the other edge, passing around the entire flake, was negligible, as determined by grounding a third contact and seeing that it had no measurable effect. In MW2, detailed studies showed that the reason V_{nl}/V_0 approaches unity at low T (Fig. 2b) is that in this particular device the conductance of edge 4–5 is suppressed more than that of the others by a ZBA, so that contact 4 becomes effectively connected only to contact 2, and 5 to 6, at low temperatures.

By analysing the variation with contact spacing in device MW3 above 150 K or at large gate voltages we were able to extract an approximate resistivity per square of the two-dimensional bulk, and a contact resistance to the bulk of ~2 k Ω (see Supplementary Information 4). However, at low temperatures the contact resistance becomes too high for this procedure. Such difficulties may be overcome in the future by doping the contacts or by finding a way to make a Corbino geometry.

Data availability. The data that support the plots within this paper and other findings of this study are available from the corresponding authors upon reasonable request.

References

- Zomer, P. J., Guimaraes, M. H. D., Brant, J. C., Tombros, N. & van Wees, B. J. Fast pick up technique for high quality heterostructures of bilayer graphene and hexagonal boron nitride. *Appl. Phys. Lett.* **105**, 013101 (2014).
- Dean, C. R. *et al.* Boron nitride substrates for high-quality graphene electronics. *Nat. Nanotech.* **5**, 722–726 (2010).